Check for updates

ADVANCED FUNCTIONAL MATERIALS
www.afm-journal.de

Defect Engineering of Ta_3N_5 Photoanodes: Enhancing Charge Transport and Photoconversion Efficiencies via Ti Doping

*Laura I. Wagner, Elise Sirotti, Oliver Brune, Gabriel Grötzner, Johanna Eichhorn, Saswati Santra, Frans Munnik, Luca Olivi, Simone Pollastri, Verena Streibel, and Ian D. Sharp**

While Ta_3N_5 shows excellent potential as a semiconductor photoanode for solar water splitting, its performance is hindered by poor charge carrier transport and trapping due to native defects that introduce electronic states deep within its bandgap. Here, it is demonstrated that controlled Ti doping of Ta_3N_5 can dramatically reduce the concentration of deep-level defects and enhance its photoelectrochemical performance, yielding a sevenfold increase in photocurrent density and a 300 mV cathodic shift in photocurrent onset potential compared to undoped material. Comprehensive characterization reveals that Ti^{4+} ions substitute Ta^{5+} lattice sites, thereby introducing compensating acceptor states, reducing the concentrations of deleterious nitrogen vacancies and reducing Ta^{3+} states, and thereby suppressing trapping and recombination. Owing to the similar ionic radii of Ti^{4+} and Ta^{5+}, substitutional doping does not introduce lattice strain or significantly affect the underlying electronic structure of the host semiconductor. Furthermore, Ti can be incorporated without increasing the oxygen donor content, thereby enabling the electrical conductivity to be tuned by over seven orders of magnitude. Thus, Ti doping of Ta_3N_5 provides a powerful basis for precisely engineering its optoelectronic characteristics and to substantially improve its functional characteristics as an advanced photoelectrode for solar fuels applications.

1. Introduction

Photoelectrochemical (PEC) water splitting has emerged as a promising approach for sustainable production of green hydrogen using solar energy. Among the various photoanode materials that have been investigated for this purpose, orthorhombic tantalum nitride (Ta_3N_5) has attracted considerable interest due to its *n*-type character, moderate bandgap of 2.1 eV, and favorable band energetics for water-splitting reactions.[1,2] However, challenges associated with poor charge transport and photocarrier recombination within this material limit its overall PEC performance.[2,3] Indeed, although the band energetics of Ta_3N_5 provide a theoretical basis for its use in spontaneous overall water splitting, these photoanodes exhibit relatively large onset potentials. Such performance limitations primarily stem from native point defects within Ta_3N_5, the most common of which are nitrogen vacancies (v_N) and reduced tantalum Ta^{3+} states.[4] Considering

L. I. Wagner, E. Sirotti, O. Brune, G. Grötzner, J. Eichhorn, S. Santra, V. Streibel, I. D. Sharp
Walter Schottky Institut
Technische Universität München
85748 Garching, Germany
E-mail: sharp@wsi.tum.de

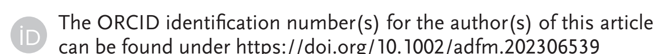

The ORCID identification number(s) for the author(s) of this article can be found under https://doi.org/10.1002/adfm.202306539

© 2023 The Authors. Advanced Functional Materials published by Wiley-VCH GmbH. This is an open access article under the terms of the Creative Commons Attribution License, which permits use, distribution and reproduction in any medium, provided the original work is properly cited.

DOI: 10.1002/adfm.202306539

L. I. Wagner, E. Sirotti, O. Brune, G. Grötzner, J. Eichhorn, S. Santra, V. Streibel, I. D. Sharp
Physics Department
TUM School of Natural Sciences
Technische Universität München
85748 Garching, Germany

F. Munnik
Institute of Ion Beam Physics and Materials Research
Helmholtz-Zentrum Dresden-Rossendorf (HZDR)
01328 Dresden, Germany

L. Olivi, S. Pollastri
Elettra–Sincrotrone Trieste S.C.p.A.
SS 14–km 163,5, Basovizza, Trieste 34149, Italy

S. Pollastri
Department of Physics, Computer Science and Mathematics
University of Modena and Reggio Emilia
Via Campi 103, Modena 41125, Italy

that most synthesis routes for Ta_3N_5 involve ammonolysis of tantalum oxide, substitutional oxygen (O_N) defects are also ubiquitous, serving as shallow donors responsible for the majority *n*-type conductivity and even playing a role in stabilizing the material.[5] Thus, the presence of O_N in moderate concentrations is generally beneficial for PEC applications. On the other hand, both v_N defects and associated Ta^{3+} centers possess energetic levels deep within the bandgap, can destabilize the compound,[5] and are associated with severe photocarrier trapping and recombination, all of which are deleterious to PEC performance characteristics.[6] Hence, developing approaches to suppress or passivate such states is crucial for improving the efficiency of Ta_3N_5 photoanodes.

To address the challenges associated with carrier transport and trapping, various strategies have been explored, including optimization of the synthesis conditions,[2,7–9] fabrication of nanostructures,[10] and construction of layered heterojunctions.[11,12] In addition, foreign atom doping has been extensively investigated and has led to remarkable performance advances. To date, a wide range of dopant elements, including Zr,[13–15] Mg,[16,17] Ge,[18] La,[19] Sc,[20] Na,[21,22] K,[21,22] Rb,[21] and Cs,[21] as well as co-doping with some of these elements,[17,19] have been explored. While several mechanisms have been proposed to describe corresponding improvements of the PEC characteristics of doped Ta_3N_5, most studies conclude that the primary role of these dopants is to modulate the concentrations and populations of native point defects (ν_N and Ta^{3+}), as well as the majority O_N donor content. A prominent example of this is Zr-doped Ta_3N_5, in which Zr^{4+} incorporates on Ta^{5+} sites (Zr_{Ta}) as a compensating electron acceptor, significantly reducing the concentrations of deep traps associated with both v_N and Ta^{3+}.[15,17] Increasing the Zr content also increases the concentration of O_N,[14] with the defect pair possessing a lower formation energy than isolated Zr_{Ta}. While this combined incorporation improves the overall performance of Ta_3N_5 photoanodes, it limits independent control over the competing defect properties of Zr_{Ta} and O_N, and potentially restricts the tunable range of bulk conductivity. Furthermore, the combination of increased unit cell volume due to the larger ionic radius of Zr^{4+} (72 pm) compared to Ta^{5+} (64 pm) and the increase of oxygen loading in the lattice leads to a slight increase of the bandgap that can reduce the overall solar energy harvesting capacity.[15]

Here, we hypothesize that Ti impurity doping can offer similar benefits as Zr in terms of eliminating deep-level defect states associated with v_N and Ta^{3+}, while also providing additional opportunities to tune the electronic conductivity without increasing the bandgap of Ta_3N_5. Indeed, while Ti and Zr lie in the same group of the periodic table, immediately to the left of Ta, the ionic radius of Ti^{4+} (61 pm) is much closer to that of Ta^{5+} than is Zr^{4+}, suggesting that the lattice parameters of Ta_3N_5 can be preserved upon substitutional Ti doping at Ta sites (Ti_{Ta}). In addition, Ti possesses a lower oxygen affinity compared to Zr, enabling the facile replacement of Ti—O with Ti—N bonds during ammonolysis, whereas Zr requires extremely low residual oxygen pressure to form a nitride.[23] While we are not aware of prior experimental investigations of Ti-doped Ta_3N_5, Fan et al.[24] recently used hybrid density functional theory (DFT) to computationally assess the role of Ti_{Ta} on the optoelectronic properties of Ta_3N_5, predicting that Ti should be a *p*-type dopant. Their calculations, which also considered the impact of simultaneous incorporation of various concentrations of O_N donors, showed that careful control of both impurity dopant types could be used to tune the Fermi level across the bandgap, as well as the band edge positions with respect to the reversible potentials for water splitting. Therefore, precise control of Ti_{Ta} and O_N within Ta_3N_5 could lead to a lowered onset potential and improved photocurrent density due to suppression of native deep-level defects.[24]

In this work, we demonstrate the successful synthesis of Ti-doped Ta_3N_5 (Ti:Ta_3N_5) thin films and experimentally investigate the effect of Ti content on the structural, optical, electrical, and photoelectrochemical properties of the material. To our best knowledge, this is the first experimental study of Ti-doped Ta_3N_5 photoanodes. Here, polycrystalline Ti:Ta_3N_5 thin films were produced by reactive co-sputtering of amorphous Ta—Ti—O layers, followed by nitridation in ammonia. This synthesis procedure yields a set of polycrystalline Ti:Ta_3N_5 films with similar thickness, crystallinity, and structure, but varying titanium content from 0 to 3 at.%. Comprehensive elemental analysis confirms the incorporation of Ti^{4+} coordinated to N, indicating the formation of Ti_{Ta}. Importantly, we verify that Ti doping preserves the lattice parameters of Ta_3N_5 and is not correlated with an increase in the bulk oxygen content, which stands in contrast to Zr doping. This compositional independence offers additional control over the optoelectronic properties of the films. Functional characterization of the photoanodes reveals significant improvements of PEC performance at low Ti concentrations (<1.5 at.%), manifesting in an up to sevenfold increase in photocurrent density and up to 300 mV decrease of the onset potential. Optoelectronic characterization indicates that these improvements result from a considerable decrease in the concentration of deep-level defects associated with v_N, leading to enhanced photocarrier transport properties and reduced carrier trapping and recombination. Electrical transport measurements confirm that Ti_{Ta} acts as a compensating acceptor and enables tuning of the electrical conductivity over seven orders of magnitude. However, under the processing conditions used in this study, there is an upper concentration limit of 1.5 at.% Ti, beyond which a metallic TiN phase forms. Overall, our results demonstrate that Ti doping is a powerful strategy for improving the optoelectronic properties of Ta_3N_5 photoanodes, suppressing deep-level defect formation, and significantly improving photoelectrochemical efficiency.

2. Results and Discussion

2.1. Controlling Substitutional Ti Doping of Ta_3N_5

Ti doped Ta_3N_5 (Ti:Ta_3N_5) thin films were synthesized by reactive magnetron co-sputtering of Ti-doped tantalum oxide (Ti:TaO_x) on both (100) n^+ Si and fused silica wafers, followed by post-deposition ammonia annealing at 940 °C for 3 h. The Ti content in the films was carefully controlled by varying the Ti sputter target power (0, 7, 15, 30, 45, and 60 W) while maintaining a constant Ta sputter target power of 60 W. Sputtering times were adjusted to achieve a uniform film thickness of 110 nm for all samples, as determined by X-ray reflectivity (XRR) measurements. We note that this thickness is well below the optimal value for achieving maximum photoelectrochemical current densities,[11] but it enables reliable nitridation with minimal composition

© 2023 The Authors. Advanced Functional Materials published by Wiley-VCH GmbH

16163028, 0, Downloaded from https://onlinelibrary.wiley.com/doi/10.1002/adfm.202306539 by University Modena, Wiley Online Library on [19/12/2023]. See the Terms and Conditions (https://onlinelibrary.wiley.com/terms-and-conditions) on Wiley Online Library for rules of use; OA articles are governed by the applicable Creative Commons License

16163028, 0, Downloaded from https://onlinelibrary.wiley.com/doi/10.1002/adfm.202306539 by University Modena, Wiley Online Library on [19/12/2023]. See the Terms and Conditions (https://onlinelibrary.wiley.com/terms-and-conditions) on Wiley Online Library for rules of use; OA articles are governed by the applicable Creative Commons License

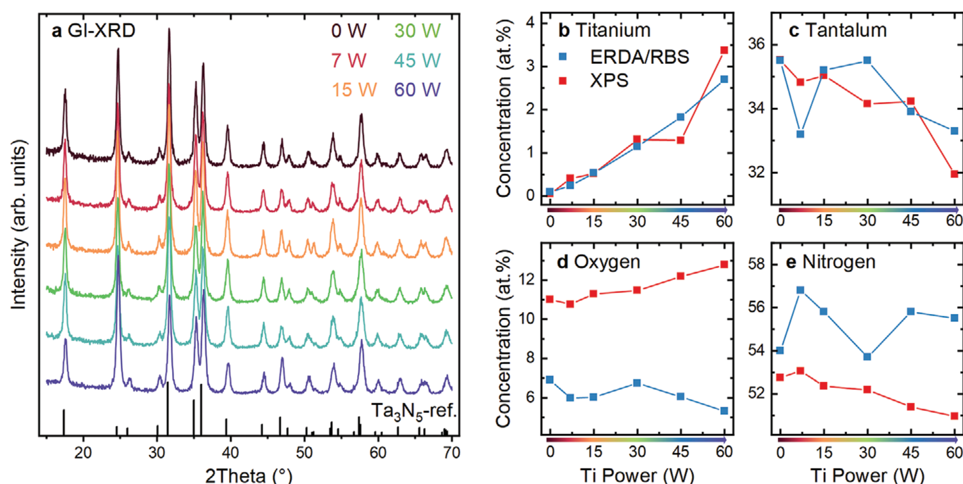

Figure 1. Structural and elemental analysis of Ti:Ta_3N_5 a) GI-XRD patterns of Ti:Ta_3N_5 thin films as a function of Ti sputter target power. All patterns match with the reference pattern (black) for orthorhombic Ta_3N_5. b–e) Atomic concentrations of the films measured with ERDA/RBS (blue) to determine the bulk composition and with XPS (red) to determine the surface composition, quantified for b) Ti, c) Ta, d) O, and e) N as a function of the Ti sputter target power.

gradients necessary for the present study of the impact of Ti doping on optoelectronic and photoelectrochemical characteristics. The film grown with 0 W Ti power was used as a pure Ta_3N_5 reference and is denoted as 0 W-Ti:Ta_3N_5, with the other films similarly labeled on the basis of the Ti sputter target power. All films exhibit a planar, polycrystalline morphology with fine porosity. Scanning electron and atomic force microscopy images can be found in the Supporting Information (Figures S1 and S2, Supporting Information).

As shown in **Figure 1**a, the grazing incidence X-ray diffraction (GI-XRD) patterns of all samples match the reference pattern of orthorhombic Ta_3N_5, irrespective of the applied Ti target power. No unidentified diffraction peaks or peak shifts are observed with varying Ti content, confirming successful synthesis of orthorhombic Ta_3N_5 thin films with similar crystallinity and lattice constants. Although XRD peak shifts are commonly observed when introducing other dopant elements, such as Zr,[15] the absence of such changes of the unit cell parameters in the present case can be attributed to the similar ionic radii of Ti^{4+} (61 pm) and Ta^{5+} (64 pm).[24] This similarity of cation sizes suggests structural compatibility, which could enable the substitutional incorporation of Ti_{Ta} as an acceptor impurity with minimal generation of local strain or modification of the basic electronic structure of the host Ta_3N_5 semiconductor.

To evaluate the bulk chemical compositions, including the concentrations of Ti and O impurities within the deposited films, elastic recoil detection analysis (ERDA) and Rutherford backscattering spectrometry (RBS) were performed, as shown in Figure 1b–e (blue). This bulk value is a result of averaging the depth profile of each element and disregarding surface and interface regions, an example of which can be found in Figure S3 (Supporting Information). A linear increase in Ti concentration is observed with increasing Ti sputter power, ranging from 0 at.% for 0 W-Ti:Ta_3N_5 to almost 3 at.% for the highest sputter power of 60 W-Ti:Ta_3N_5 (Figure 1b). This increase in Ti content is accompanied by a general decrease in Ta content, which would be expected in the case of Ti_{Ta} incorporation (Figure 1c). Furthermore, a decrease in bulk O content is observed as the Ti concentration is increased (Figure 1d). This observation contrasts with previous studies of Zr-doped Ta_3N_5, where the introduction of Zr impurities favored the simultaneous formation of Zr_{Ta} and O_N as compensating acceptor and donor defects, respectively.[14,15,17] This important difference between Ti and Zr is likely due to the significantly higher oxygen affinity of Zr compared to Ti.[23]

In addition to the Ti and O impurity concentrations, the N content is a crucial parameter since nitrogen vacancies (v_N) are known to be deep donors that act as deleterious recombination centers in Ta_3N_5. The nitrogen content remains within 54–57 at.% for all samples (Figure 1e). All films, except for the 7 W-Ti:Ta_3N_5, exhibit a nitrogen deficiency, with N/(Ti+Ta) ratios ranging from 1.47 to 1.56, suggesting the presence of v_N native defect centers. However, 7 W-Ti:Ta_3N_5 exhibits a nearly stoichiometric nitrogen content, with a N/(Ti+Ta) ratio of 1.69 that compares favorably with the ideal anion-to-cation ratio of 1.66 in Ta_3N_5. While the nearly ideal value observed in 7 W-Ti:Ta_3N_5 suggests a suppression of undesired v_N centers, it is important to note that a perfect stoichiometric ratio does not necessarily indicate the absence of nitrogen impurities, since atomic or molecular nitrogen interstitials can be trapped within the polycrystalline film during synthesis.[25] Thus, optical characterization of defect-related sub-bandgap absorption was performed, as discussed below.

We next assessed the influence of Ti incorporation on the surface composition by performing X-ray photoelectron spectroscopy (XPS) on all films (Figure 1b–e, shown in red). A complete table of ERDA/RBS and XPS results can be found in Table S1 (Supporting Information). The most significant variation between the bulk and surface composition is observed for the oxygen and nitrogen contributions. The surfaces of all samples exhibit a higher oxygen content of ≈11–13 at.%, compared to the bulk concentration of only 5–7 at.%. Correspondingly, the nitrogen concentration at the surface (51–53 at.%) is lower than in the bulk (54–57 at.%). This observation is consistent with the formation of a few nanometer thick native oxide

© 2023 The Authors. Advanced Functional Materials published by Wiley-VCH GmbH

16163028, 0, Downloaded from https://onlinelibrary.wiley.com/doi/10.1002/adfm.202306539 by University Modena, Wiley Online Library on [19/12/2023]. See the Terms and Conditions (https://onlinelibrary.wiley.com/terms-and-conditions) on Wiley Online Library for rules of use; OA articles are governed by the applicable Creative Commons License

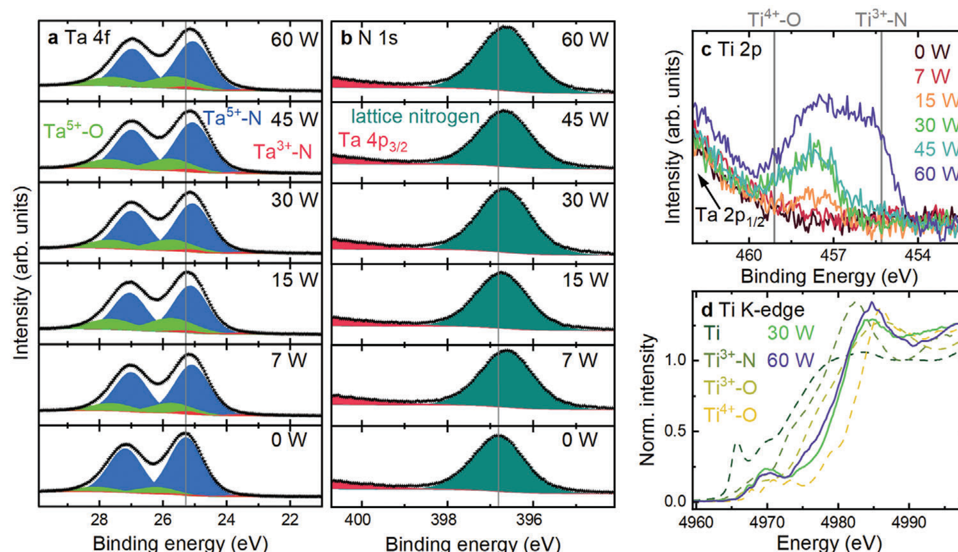

Figure 2. X-ray photoelectron spectra from a) Ta 4f, b) N 1s, and c) Ti 2p core level regions for the differently doped Ti:Ta_3N_5 thin films. d) Fluorescence yield of X-ray absorption near edge structure (XANES) at the Ti K-edge for the 30 and 60 W Ti power samples (solid lines), compared to Ti-containing reference samples with different oxidation states (dotted lines): Ti from Ti metal, Ti^{3+}—N from TiN, Ti^{3+}—O from Ti_2O_3, and Ti^{4+}—O from anatase-type TiO_2.

layer, which is commonly observed for nitrides exposed to ambient atmosphere.[7,8,26] The increasing surface oxygen enrichment with increasing Ti concentration suggests that doping leads to a slight increase in the thickness of this oxidic overlayer. Nevertheless, a significant lattice nitrogen contribution was observed with XPS, indicating that the surface oxide layer remains thin, on the order of a few nanometers.

The Ta 4f core level spectra (**Figure 2**a) exhibit two clear peaks centered near 25.3 and 27.2 eV, which can be deconvoluted into three spin–orbit-splitting doublet contributions from Ta^{3+}—N, Ta^{5+}—N, and Ta^{5+}—O bonding at progressively increasing binding energies.[19] At the surface only 1.8 to 2.8% of all tantalum atoms are observed in the reduced Ta^{3+}—N state. We link this very low reduced Ta^{3+} defect concentration to the use of a fully oxidized Ti:TaO_x precursor. As indicated above, the native oxide surface layer is thin and all spectra are dominated by Ta^{5+}—N bonding within the lattice of Ta_3N_5, as also evidenced by the prominent N 1s core level peak near 396.8 eV (Figure 2b). Notably, both the Ta 4f and N 1s core level binding energies of the Ti:Ta_3N_5 exhibit a spectral redshift of ≈ -0.2 eV compared to the undoped 0 W-Ti:Ta_3N_5. This shift in binding energy for both elemental constituents indicates a displacement of the Fermi level towards the valence band edge, which is consistent with the role of Ti as a compensating electronic acceptor in Ta_3N_5.

To further investigate the electronic state of Ti within Ta_3N_5, we performed a detailed analysis of both its XPS and X-ray absorption near edge structure (XANES) spectra, which provide insight into the local bonding and coordination environment. Figure 2c displays the Ti 2p spectral region, which overlaps strongly with the Ta $4p_{1/2}$ XPS signal, making reliable quantification challenging. Nevertheless, we observe the expected increase in Ti signal with increasing sputter power at a peak position that does not match either Ti^{4+}—O or Ti^{3+}—N for low Ti concentrations. For 45 W-Ti:Ta_3N_5 and 60 W-Ti:Ta_3N_5 a second peak corresponding to Ti^{3+}—N arises. Similarly, a small contribution from Ti^{4+}—O emerges for higher Ti concentrations (≥1.5 at.%, ≥ 30 W) and could be related to the formation of an increasingly thicker surface oxide.

To verify the isostructural incorporation of Ti into the Ta_3N_5 lattice, we conducted Ti K-edge XANES measurements (Figure 2d), which are sensitive to the oxidation state and coordinating species of Ti.[27] To aid in the interpretation of the Ti:Ta_3N_5 film measurements, we first compared them to a series of materials possessing different Ti oxidation states and bonding partners, either directly measured at the XAFS beamline (Elettra) or taken from literature, namely Ti in elemental Ti metal, octahedral Ti^{3+}—N in TiN,[28] octahedral Ti^{3+}—O in Ti_2O_3, and distorted octahedral Ti^{4+}—O in anatase TiO_2. We were unable to obtain an experimental reference for Ti^{4+}—N since the relevant compound, Ti_3N_4, is only stable at high pressures and high temperatures.[29] Nevertheless, as expected, the reference measurements display the well-known shift of absorption edge position to higher X-ray energies with increasing Ti oxidation state. In addition, for a constant oxidation state, the edge position shifts to higher energies when the bonding partner changes from nitrogen to oxygen, reflecting the electronegativity difference between the two anions.

Isostructurally incorporated Ti_{Ta} in Ta_3N_5 is expected to possess its maximum oxidation state of 4+ and to be coordinated with nitrogen atoms. According to the energetic sequence observed in the reference measurements described above, such Ti species should exhibit an absorption edge that lies between those of Ti^{3+}—O and Ti^{4+}—O. Indeed, we observe that this is the case for the absorption edges of 30 W-Ti:Ta_3N_5 and 60 W-Ti:Ta_3N_5 (Figure 2d), providing strong evidence for substitutional incorporation of Ti on Ta lattice sites, bonded to nitrogen within the first coordination shell. However, upon closer inspection, we also observe a slight decrease in the edge energy and a stronger absorption intensity immediately below the edge at 4975 eV for

© 2023 The Authors. Advanced Functional Materials published by Wiley-VCH GmbH

16163028, 0, Downloaded from https://onlinelibrary.wiley.com/doi/10.1002/adfm.202306539 by University Modena, Wiley Online Library on [19/12/2023]. See the Terms and Conditions (https://onlinelibrary.wiley.com/terms-and-conditions) on Wiley Online Library for rules of use; OA articles are governed by the applicable Creative Commons License

60 W-Ti:Ta_3N_5 compared to 30 W-Ti:Ta_3N_5. This observation suggests a decreased oxidation state for at least a fraction of the Ti atoms in films with high Ti content, which is consistent with the emergence of a low binding energy feature in the Ti 2p XPS spectra (Figure 2c). Thus, we can conclude that Ti can be substitutionally doped on Ta sites in orthorhombic Ta_3N_5 at low Ti concentrations (≤1.5 at.% and ≤30 W). In such cases, Ti is in its maximum oxidation state of 4+ and is primarily coordinated with N. By contrast, at higher Ti contents (>1.5 at.%, >45 W), a TiN-like defect phase emerges, either in an amorphous state or at concentrations too low to be detected via GI-XRD. Finally, it is worth noting that TiN is metallic. While such a phase could enhance the overall film conductivity, it also possesses a large density of states at the Fermi level, which could contribute to accelerated photocarrier recombination. Thus, TiN formation is likely to have a detrimental effect on photoelectrode function, and Ti doping concentrations should therefore be maintained below the apparent solubility limit of ≈1.5 at.% in Ta_3N_5.

2.2. Enhancing Photoelectrochemical Characteristics of Ti:Ta_3N_5

Having successfully verified the synthesis of Ti-doped Ta_3N_5 thin films, we now turn to evaluation of their PEC characteristics. These measurements were first conducted in a 1 M KP_i buffer at pH 12.3 with 0.1 M $K_4Fe(CN)_6$ as a sacrificial reagent (**Figure 3**a–c; Figure S4, Supporting Information). The sacrificial hole acceptor is necessary to ensure the collection of all charge carriers reaching the semiconductor-electrolyte junction, thereby allowing an assessment of the fundamental impact of doping on the photoanode efficiency without influence from electrocatalytic limitations. We find that all Ti:Ta_3N_5 electrodes are similarly stable under constant potential and illumination (Figure 3b), with no degradation observed over a 1 h chronoamperometric test (Figure S4c, Supporting Information). Extended stability testing of a representative 7 W-Ti:Ta_3N_5 film for 14 h revealed retention of ≈80% of the original photocurrent density at 1.23 V versus RHE (Figure S5, Supporting Information), with the small decline of current associated with mild oxidation of the surface (Figure S6, Supporting Information). Considering that no change of crystalline structure, thickness, or morphology was observed during the test (Figures S7 and S8, Supporting Information), we conclude that the measured photocurrents are due to oxidation of the sacrificial reagent rather than corrosion of the samples.

Notably, the different Ti:Ta_3N_5 films exhibit considerably different photocurrent densities as a function of Ti concentration. With the exception of the highest Ti content film (60 W-Ti:Ta_3N_5), all Ti-doped Ta_3N_5 photoanodes show improved photocurrent densities compared to the undoped (0 W-Ti:Ta_3N_5) material (Figure 3a,b). Similarly, the photocurrent onset potential, defined here as the potential at which a current density of 0.05 mA cm^{-2} is exceeded, exhibits a clear decrease for all but the highest doping concentration (Figure 3c). However, it is important to note that these performance metrics do not increase monotonically with Ti content. Rather, the sample with the lowest doping concentration (7 W-Ti:Ta_3N_5) performed the best among the evaluated thin film photoanodes. Compared to the undoped film (0 W-Ti:Ta_3N_5), this sample displays a remarkable sevenfold increase in photocurrent density at 1.23 V versus RHE and

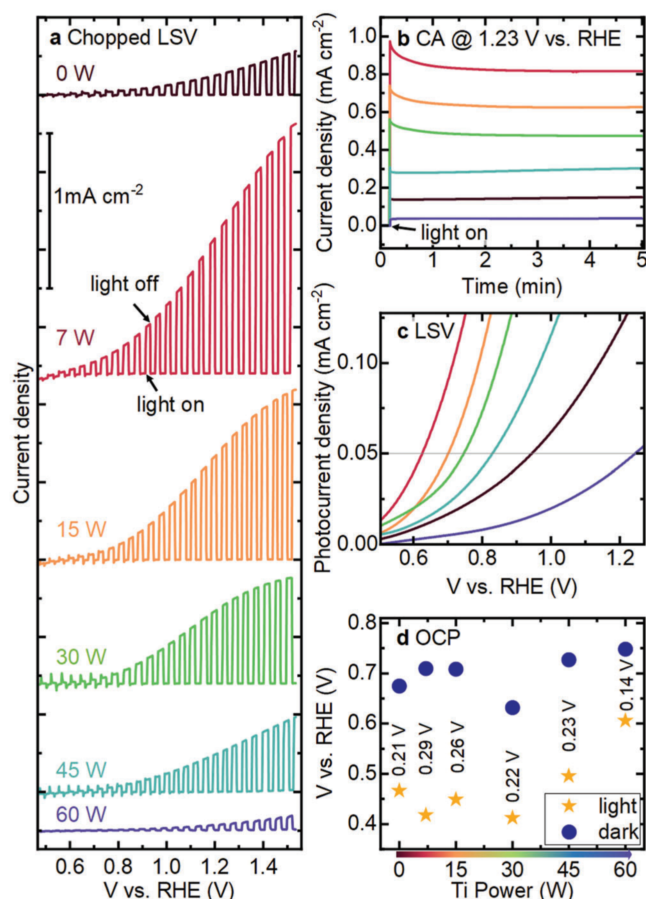

Figure 3. Photoelectrochemical measurements of Ti:Ta_3N_5 photoanodes as a function of Ti content in 1 M KP_i buffer at pH 12.3 with 0.1 M $FeK_4(CN)_6$ added as a sacrificial reagent. a) Linear sweep voltammetry (LSV) data obtained at a sweep rate of 20 mV s^{-1} with chopped AM 1.5G illumination at 100 mW cm^{-2}. b) Chronoamperometry (CA) performed at 1.23 V versus RHE under simulated AM 1.5G illumination at 100 mW cm^{-2}. c) Analysis of the photocurrent onset potential obtained during LSV under constant illumination. A photocurrent density of 0.05 mA cm^{-2} is used to estimate the onset potential. The color code for the data sets in (b,c) is the same as in (a). d) Open circuit potential (OCP) under equilibrium conditions taken before the first LSV scan in dark and under AM 1.5G illumination at 100 mW cm^{-2}. The corresponding photovoltage, estimated as the difference of OCP under illumination and in darkness, is provided for each sample.

a 300 mV reduction in the onset potential. In addition, we reiterate that the film thickness of 110 nm used here for fundamental investigations of Ti doping is significantly thinner than the known optimal value of ≈800 nm for achieving maximum photoelectrochemical performance. While absolute performance optimization is outside the scope of the present work, initial experiments using a 250 nm thick 0.4 at.% Ti-doped film revealed a significant increase in photocurrent, as shown in Figure S9 (Supporting Information). This finding indicates that future strategies for optimizing film thickness and nitridation conditions are likely to yield even greater performance from Ti:Ta_3N_5.

By repeating the PEC measurement procedure in the absence of sacrificial hole acceptor, we were able to further assess the impact of Ti doping on photoanode performance characteris-

© 2023 The Authors. Advanced Functional Materials published by Wiley-VCH GmbH

tics (Figure S4, Supporting Information). As expected, when no sacrificial reagent or catalyst is present, all Ti:Ta_3N_5 photoanodes exhibited lower current densities, with a maximum value of 0.18 mA cm^{-2} at 1.23 V versus RHE achieved for both of the lightly doped films, 7 and 15 W-Ti:Ta_3N_5. By comparing the *J*–*E* curves obtained with and without sacrificial reagent, as well as considering the thin film optical properties (discussed below), we then quantified the charge separation and charge injection efficiencies for each of the Ti:Ta_3N_5 films (Figure S4d,e, Supporting Information). This analysis reveals that Ti doping leads to a beneficial enhancement of the charge separation efficiency, which is particularly pronounced for low Ti doping concentrations. In contrast, Ti doping appears to generally reduce the interfacial injection efficiency, which could be a consequence of surface oxide formation, though no systematic trend with composition was observed. Overall, these findings indicate that the increased PEC performance of Ti-doped Ta_3N_5 originates from improved charge separation and photocarrier transport rather than improved catalytic efficiency.

To gain further insight into the reduced onset potential observed for low Ti doping concentrations, we analyzed the open circuit potentials (OCPs) of each photoanode under both darkness and illumination, as shown in Figure 3d. As expected for n-type photoanodes, illumination leads to a decrease in the OCP for all investigated samples. The difference between the dark and illuminated OCP provides an approximate measure of the photovoltage, which is influenced by the interfacial energetic alignment at the semiconductor|electrolyte interface and the accumulated charge carrier concentration under flat band conditions, which is itself enhanced by improved carrier transport and suppressed recombination rates.[20,30] In all doped samples, except for the highest Ti doping concentration (60 W-Ti:Ta_3N_5), larger photovoltages were observed compared to the undoped 0 W-Ti:Ta_3N_5 reference film.

Previously, Fan and co-workers[24] predicted that Ti and O incorporation in Ta_3N_5 can alter the band edge positions relative to the reversible potentials for water splitting reactions, with increasing Ti (increasing O) leading to negative (positive) shifts of the band positions. However, we do not observe systematic trends in either dark or illuminated OCP with Ti doping. Instead, improved photovoltage generation is more directly correlated with increased photocurrent densities. This finding suggests that the enhanced performance is more likely due to improved charge carrier transport and the suppression of trapping and recombination at defect sites, rather than more favorable interfacial energetics. This assignment is also consistent with the dominant influence of interfacial oxygen, which is believed to create a large surface dipole that is responsible for the commonly observed anodic shift of onset potentials in Ta_3N_5 photoanodes,[25] thereby inhibiting spontaneous overall water splitting.

2.3. Tailoring Optoelectronic Properties of Ti:Ta_3N_5

In order to investigate the role of charge trapping and recombination at defects on the dynamics of surface band bending under illumination, we used contact potential difference (CPD) measurements to examine the time evolution of the surface photovoltage (SPV) in Ti:Ta_3N_5. When illuminated with above bandgap radiation using a 455 nm LED, all Ti:Ta_3N_5 films displayed a negative SPV, consistent with their n-type character (**Figure 4**a). However, significant differences were observed in both the magnitude and time constants of the SPV responses as a function of Ti content. In particular, lightly doped Ti:Ta_3N_5 (≤1.5 at.% and ≤30 W) exhibited larger photovoltages (>250 meV) compared to both the undoped and the heavily doped Ta_3N_5. This observation is in good agreement with the OCP analysis presented earlier (Figure 3d), indicating that high Ti doping concentrations lead to reduced photoactivity, most likely due to nucleation of a secondary metallic TiN phase. In addition to the absolute magnitude of the SPV, the Ti-doped thin films show a markedly faster transient response to changes in illumination conditions compared to undoped Ta_3N_5. The more rapid establishment of steady–state SPV values, especially during relaxation to the dark state, can typically be related to improved minority carrier diffusion and reduced carrier trapping.[19] Hence, these SPV measurements indicate that Ti doping leads to improved optoelectronic quality and charge separation at the surface, which correlates with improved PEC activity.

At this point, we have established that Ti-doped Ta_3N_5 exhibits improved photocurrent densities, reduced onset potentials, and enhanced charge separation efficiencies compared to the undoped material, and that there exists an optimal range for this doping concentration. These benefits are consistent with enhanced charge carrier transport and suppressed recombination below a certain threshold at which a secondary TiN phase appears to form. To shed additional light on the underlying origin of this behavior, we characterized the optical properties of Ti:Ta_3N_5. Figure 4b shows the optical absorption spectra of Ti:Ta_3N_5 films deposited on fused silica. All samples exhibit a similar indirect bandgap of ≈2.1 eV (Figure S10, Supporting Information), consistent with our previous assignment[7] and matching their orange appearance (Figure 4b, inset photo). The observation that the bandgap is independent of Ti content can be attributed to the similar ionic radii of Ti^{4+} and Ta^{5+}, which results in constant unit cell parameters, as discussed in the context of the XRD analysis presented above. Thus, the electronic structure and orbital overlap are only weakly affected by Ti doping across the investigated composition range and changes in PEC activity are not due to different light-harvesting capabilities of the films. Rather, they appear to arise from the tunable defect properties within Ti:Ta_3N_5.

Importantly, we observe dramatic changes in the sub-bandgap optical absorption as a function of Ti dopant concentration. In particular, we find a decrease in the absorption coefficient in this spectral range (<2.0 eV) by at least one order of magnitude for the lowest Ti content (7 W-Ti:Ta_3N_5) compared to undoped material, indicating a substantial reduction of optically active defects upon the introduction of Ti dopants. Overall, the sub-bandgap optical response is decreased for all films containing ≤1.5 at.% Ti (≤30 W Ti power). Previous reports have attributed this sub-bandgap absorption to electronically active deep-level defects that serve as sites for trapping and recombination, most notably v_N and Ta^{3+} centers.[4] Low-temperature photoluminescence (PL) spectroscopy of these lightly doped films confirms a significant decrease in emission from such defect states compared to the undoped material (Figure S11, Supporting Information). Thus, we can conclude that a primary impact of Ti compensation doping of Ta_3N_5 is the suppression of deep-level native defect states,

© 2023 The Authors. Advanced Functional Materials published by Wiley-VCH GmbH

16163028, 0, Downloaded from https://onlinelibrary.wiley.com/doi/10.1002/adfm.202306539 by University Modena, Wiley Online Library on [19/12/2023]. See the Terms and Conditions (https://onlinelibrary.wiley.com/terms-and-conditions) on Wiley Online Library for rules of use; OA articles are governed by the applicable Creative Commons License

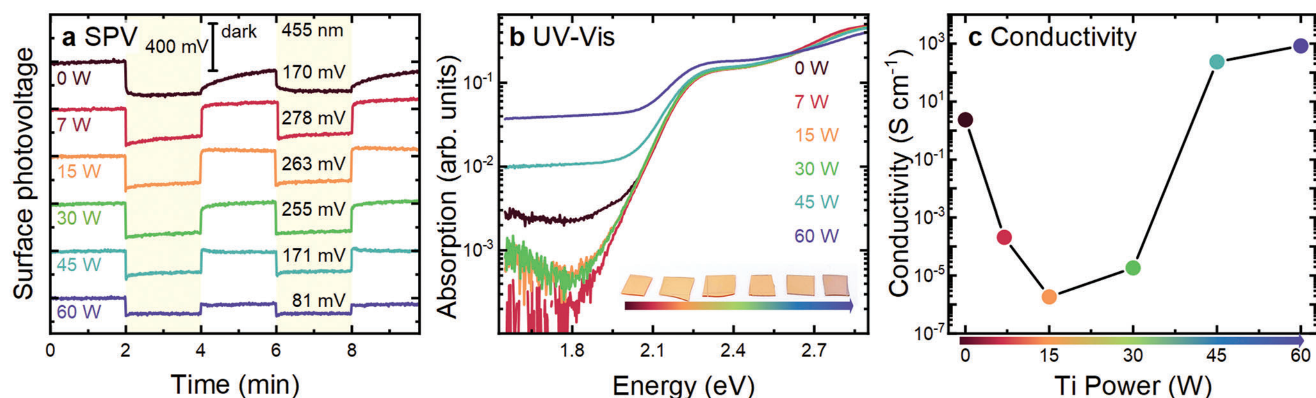

Figure 4. Optoelectronic properties of Ti:Ta_3N_5 a) Time evolution of the surface photovoltage (SPV) measured as the change of the contact potential difference (CPD) during repeated cycling from dark to illumination conditions with a 455 nm LED. b) Optical absorption spectra, showing significant changes of the sub-bandgap response as a function of Ti doping levels within Ti:Ta_3N_5. The inset shows a photograph of the respective films, which darken at high Ti content due to broad spectral absorption by a secondary TiN phase. c) Electrical conductivity of Ti:Ta_3N_5 measured in darkness, which initially decreases due to compensation by Ti acceptors and then increases due to formation of metallic TiN.

which leads to a significant improvement of the PEC activity in terms of both enhanced photocurrent generation and improved onset potential (Figure 3a,c). We note that a similar phenomenon has also been observed with Zr doping, which is not surprising given that both elements belong to the same group and possess identical oxidation states (Ti^{4+} and Zr^{4+}). However, we have also shown that the weaker oxygen affinity of Ti allows its incorporation largely independent of oxygen, which is not the case for Zr and offers new prospects for independent control over the impurity concentrations of electronically active defects.

In contrast to the significant reduction of sub-bandgap optical absorption observed for lightly Ti-doped films (≤1.5 at.%, ≤30 W), higher Ti concentrations (>1.5 at%, >30 W) result in a pronounced increase of sub-bandgap optical absorption. The sub-bandgap absorption coefficient increases with increasing Ti content for concentrations above 1.5 at.%, leading to a visible darkening of the films (Figure 4b, inset). This observation is consistent with elemental analysis via XAS and XPS discussed above (Figure 2), which revealed the emergence of Ti^{3+}—N bonding and formation of a metallic TiN impurity phase at higher Ti content that is detrimental to PEC activity. Thus, the increasing sub-bandgap absorption above 1.5 at.% Ti provides another indication for the solubility limit of isostructurally incorporated Ti_{Ta} acceptors, beyond which metallic TiN formation is favored.

Measurements of the in-plane electrical conductivity provide valuable insights into the role of Ti doping on the functional characteristics of Ti:Ta_3N_5 photoanodes and further indicate that changes of the sub-bandgap optical absorption are accompanied by substantial changes to the electrical transport characteristics. As shown in Figure 4c, the electrical conductivity decreases by several orders of magnitude upon the introduction of small concentrations of Ti. In particular, the undoped films exhibit an electrical conductivity of 2.4 S cm^{-1}, which decreases to 2.1×10^{-4} and 1.8×10^{-6} S cm^{-1} for 7 W- and 15 W-Ti:Ta_3N_5 films, respectively. This dramatic decrease is consistent with the expected behavior of Ti_{Ta} as an acceptor state that compensates majority of donor defects. Indeed, as discussed in the context of optical characterization, we also observe a decrease in the oxygen donor (O_N) and nitrogen-vacancy (ν_N) concentrations at low Ti concentrations. Thus, Ti doping serves a dual role by electronically compensating those donor states that are present, while simultaneously decreasing their total concentrations within the films. The consequence is a decrease of the majority electron concentration, and thus the electrical conductivity. Moreover, the elimination of v_N is expected to reduce carrier trapping, prolong excited state lifetimes, and increase carrier mobilities. While the polycrystalline nature of our Ti-doped films and their large impedances pose challenges for Hall effect measurements, future investigations focusing on direct determination of carrier mobilities would provide additional valuable information.

At even higher Ti concentrations (>1.5 at.%, >30 W Ti power), the conductivity increases compared to that of the undoped material. This increase is directly correlated with the emergence of enhanced sub-bandgap optical absorption and Ti^{3+}-N bonding, which is consistent with the formation of a secondary TiN impurity phase. Due to its metallic nature, this phase exhibits broadband optical absorption, increases the dark conductivity of films, and leads to considerable loss of PEC activity due to enhanced recombination. Thus, for the processing conditions utilized in this study, the solubility limit of Ti is restricted to ≈1.5 at.%. However, below this threshold, Ti doping can be employed to dramatically improve the performance of Ta_3N_5 photoanodes.

3. Conclusion

In conclusion, we have demonstrated that Ti doping can significantly improve the performance of Ta_3N_5 photoanodes for application in photoelectrochemical water splitting. Using reactive co-sputtering to precisely tune Ti dopant concentrations, we systematically investigated the compositional, structural, optical, and electrical characteristics of these films. Our results indicate that Ti^{4+} can be substitutionally incorporated at Ta^{5+} lattice sites (Ti_{Ta}), acting as an electronic acceptor that compensates ubiquitous donor states in Ta_3N_5, while also reducing the concentrations of deep nitrogen vacancies, v_N. As a result, Ti-doped Ta_3N_5 exhibits dramatically enhanced photocurrent densities (up to sevenfold), lowered onset potentials (up to −300 mV), and improved charge separation efficiencies compared to the undoped material.

© 2023 The Authors. Advanced Functional Materials published by Wiley-VCH GmbH

16163028, 0, Downloaded from https://onlinelibrary.wiley.com/doi/10.1002/adfm.202306539 by University Modena, Wiley Online Library on [19/12/2023]. See the Terms and Conditions (https://onlinelibrary.wiley.com/terms-and-conditions) on Wiley Online Library for rules of use; OA articles are governed by the applicable Creative Commons License

While this behavior is similar to what has been observed for Zr-doped Ta_3N_5, Ti offers several important benefits. In particular, Ti^{4+} and Ta^{5+} share similar ionic radii, resulting in substitutional incorporation with no detectable change of the lattice parameters or electronic structure of the host semiconductor. In addition, the weaker oxygen affinity of Ti compared to Zr enables Ti doping independent of the oxygen impurity content in the films, whereas Zr doping is necessarily associated with increasing oxygen concentrations. Thus, we believe that Ti doping provides additional versatility for engineering defect properties and majority carrier concentrations. This hypothesis was confirmed by in-plane electrical transport measurements, which revealed that Ti doping can be used to modulate the electrical conductivity by up to seven orders of magnitude. The extremely low conductivities of moderately Ti-doped films indicate significant compensation of donor states, though n-type conduction was observed in all cases. Considering that v_N are significantly suppressed at these Ti concentrations, we attribute this n-type character to residual O_N impurities, as well as the solubility limit of ≈1.5 at.% Ti under the ammonolysis conditions used in this study. However, considering the differing oxygen affinities and Gibbs free energies for nitridation of tantalum and titanium,[23] an optimized synthesis strategy might enable even higher titanium incorporation without metallic TiN-like defect phases, perhaps even permitting p-type conductivity and exploration of Ta_3N_5-based photocathodes or homojunction-based electrodes in the future.

Finally, we emphasize that the focus of the present work was on a fundamental understanding of the role of Ti doping on the optoelectronic properties and photoelectrochemical characteristics of Ta_3N_5, rather than on overall energy conversion efficiency optimization. For this purpose, comparatively thin films of 110 nm were selected, which enabled reliable nitridation with minimal composition gradients. However, this is well below the optimal thickness for photocurrent generation by Ta_3N_5 photoanodes, which has been found to be ≈800 nm.[11] Indeed, initial experiments using a 250 nm thick Ti-doped (0.4 at.%) film yielded a dramatic increase in photocurrent density (Figure S9, Supporting Information). Considering the advantages of Ti doping identified in this work, a clear route to achieve maximum efficiencies and enhance performance includes the use of thicker films, optimization of ammonia annealing conditions, back contact engineering, and catalyst integration. Indeed, paired with the large availability and non-toxic character of titanium, further optimization of Ti-doped nitride photoanodes could lead to efficient synthesis of hydrogen from sunlight for a clean and sustainable future.

4. Experimental Section

Synthesis of Ti:Ta_3N_5 Thin Films: The thin films were deposited using reactive magnetron sputtering on single-side polished n^+-doped silicon (Siegert Wafer, Prime) with a resistivity below 0.005 Ω cm and on double-side polished fused silica (Siegert Wafer, Corning 7980). The use of both substrates enabled measurements requiring either insulating, transparent, or conducting substrates. In particular, XRD, XPS, PEC, and SPV were performed on n^+-Si, while XANES, UV–vis, and conductivity were probed on fused silica. Prior to deposition, all substrates were cleaned by thorough and consecutive rinsing with DI water, acetone, and isopropanol.

All films were sputtered using a Kurt. J. Lesker Company (KJLC) PVD 75 system with a base pressure of 5×10^{-8} Torr and a 17 cm distance between the 2″-targets and the substrate. The Ti—Ta—O layers were deposited at a substrate temperature of 600 °C and under constant substrate rotation of 10 rpm to ensure film uniformity. Before each deposition, the Ta (99.95% purity, KJLC) and Ti targets (99.995% purity, KJLC) were first conditioned by Ar plasma sputtering (99.9999% Ar, Linde GmbH) at a pressure of 8.5 mTorr and a DC sputtering power of 60 W for 10 min. During the second half of that time, an additional radio frequency substrate bias of 20 W was applied to clean the substrates via mild Ar ion bombardment immediately prior to deposition. In the next step, the Ti power was turned off and the substrate shutter opened for 2 min, during which an ≈5 nm thick Ta interlayer was deposited. This layer prevented Si substrates from oxidizing during the subsequent deposition step, in which a 90% Ar/10% O_2 (99.9999% O_2, Linde Electronics GmbH) process gas was introduced into the chamber at a controlled constant pressure of 8.5 mTorr. The corresponding gas flow rates were ≈37 sccm of Ar and 4 sccm of O_2. For film deposition, a constant 60 W power was supplied to the Ta target, while a series of powers from 0 to 60 W were applied to the Ti target. The Ti-doped TaO_x film deposition was initiated by opening the substrate shutter after the applied voltages and currents to both targets had stabilized. To achieve uniform film thickness for all Ti contents, the deposition time was varied from 21.5 to 25 min to account for the variation of sputter rate with Ti target power, resulting in a constant 110 nm film thickness for all samples, as confirmed by X-ray reflectivity (XRR).

Following deposition, all samples were annealed in a quartz tube furnace (Nabertherm RS 80/300/1) with a constant 100 sccm flow of NH_3 (Linde Electronics GmbH, 99.999%) at ambient pressure. Prior to annealing, the tube was alternatingly pumped and purged with N_2, to remove oxygen, as well as water adsorbed on the internal surfaces of the furnace. Then, NH_3 flow was introduced, and the temperature was ramped up with a rate of 30 K min^{-1}, held at 920 °C for 3 h, actual sample temperature was 940 °C, and left to naturally cool. To accelerate the cooling process, the clam-shell furnace was opened once the temperature had dropped below 500 °C. Once the system had reached room temperature, the furnace was purged for 20 min with pure N_2 to allow safe unloading of samples.

Material Characterization: Film thickness and structure were investigated with X-ray diffraction using a Rigaku SmartLab diffractometer equipped with a copper anode and a HyPix-3000 2D detector. Grazing incidence X-ray diffraction was measured at a fixed incidence angle of $\omega = 0.4°$, while scanning 2θ from 15° to 70° at a scan rate of 2°min^{-1} with a step size of 0.04°. XRR was measured using the same instrument by performing a 2θ-ω scan from 0 to 2.5°.

X-ray photoelectron spectroscopy was performed at a pass energy of 20 eV and a take-off angle of 0° using a SPECS System equipped with a non-monochromatized Al Kα ($h\nu$ = 1486.6 eV) source and a PHOIBOS 100 concentric hemispherical energy analyzer with an MCD-5 detector. Data analysis was performed with the CasaXPS software using a Shirley background and GL(30) peak shapes. Due to the very low carbon contamination, no energy calibration was performed apart from the intrinsic calibration of the detector. All samples were measured one after another but with no systematic order and no evidence for sample charging was observed.

Elastic recoil detection analysis and Rutherford backscattering spectrometry were both measured at the Ion Beam Centre of the Helmholtz–Zentrum Dresden-Rossendorf. For ERDA a 43 MeV Cl^{7+} ion beam was used and the angle between the sample normal and the incoming beam was fixed at 75°, with a scattering angle of 30°. The analyzed area was ≈2 × 2 mm^2. The recoil atoms and scattered ions were detected with a Bragg ionization chamber, which enabled energy measurement and Z identification of the particles. H recoils were detected with a separate solid–state detector at a scattering angle of 40°. This detector was preceded by a 25 µm Kapton foil to stop scattered ions and heavy recoil ions. The depth resolution of this system was reduced because of energy loss straggling in the foil. For RBS measurements, which allowed more accurate determination of the Ti concentration, a normal incidence 1.7 MeV He^+ ion beam was used, and the scattering angle was 170°. The circular analyzed area was 1.25 mm in diameter. Data analysis of both measurements combined was conducted using the Windf v9.3 g software.[31]

© 2023 The Authors. Advanced Functional Materials published by Wiley-VCH GmbH

16163028, 0, Downloaded from https://onlinelibrary.wiley.com/doi/10.1002/adfm.202306539 by University Modena, Wiley Online Library on [19/12/2023]. See the Terms and Conditions (https://onlinelibrary.wiley.com/terms-and-conditions) on Wiley Online Library for rules of use; OA articles are governed by the applicable Creative Commons License

X-ray absorption near edge structure measurements were performed at the XAFS beamline[32] at the Elettra Synchrotron Trieste (Italy). The storage ring was operated at 2.0 GeV in top-up mode with a typical current of 300 mA. Data were recorded at the Ti K-edge in fluorescence mode using a silicon drift detector of 80 mm^2 active area (AXAS-M, Ketek, Munich, Germany). A reference Ti foil was measured in transmission mode for energy calibration of the monochromator, composed by a fixed exit double Si (111) crystals.

Photoelectrochemical measurements were performed using a Biologic (SP-300) potentiostat in a three-electrode configuration comprising a Ag/AgCl reference electrode (3 M KCl), a Pt wire counter electrode, and the Ti:Ta_3N_5 thin film on n^+-Si as the working electrode. The experiments were conducted in a 1 M KP_i buffer at pH 12.3 with and without 0.1 M $K_4Fe(CN)_6$ present as a sacrificial hole acceptor. Before measurements, the electrolyte was purged with Ar gas (99.9999% Ar, Linde GmbH) for 15 min. Linear sweep voltammetry (LSV) was performed by scanning from 0.4 to 1.6 V versus RHE and chronoamperometry was conducted at a fixed electrochemical potential of 1.23 V versus RHE. An LED-based solar simulator (AM 1.5G, G2V Pico) adjusted to 100 mW cm^{-2} was used for illumination. The measurement sequence was: LSV in dark (50 mV s^{-1}), LSV under illumination (50 mV s^{-1}), LSV with manually chopped illumination (20 mV s^{-1}), and chronoamperometry at 1.23 V versus RHE in light for 5 min, all with $K_4Fe(CN)_6$ present. Afterward, the same procedure was repeated using fresh electrolytes without the hole scavenger present. Charge injection and separation efficiencies were calculated according to the procedure described elsewhere.[33]

The optical absorption characteristics were measured via the transflectance signal obtained with the diffuse reflectance accessories of a commercial Agilent Cary 5000 spectrophotometer using a photomultiplier tube detector. The probing light from a tungsten lamp was scanned from 800 to 300 nm with a scan speed of 60 nm min^{-1}. Photoluminescence spectroscopy was performed with a home-built system using an excitation wavelength of 532 nm. All measurements were performed in vacuum (10^{-4} mbar) at temperatures ranging from 10 K to 290 K on Ti:Ta_3N_5 on fused silica substrates. The emitted light was collected with an Olympus LUCPlanFL (NA ¼ 0.45) objective and analyzed with a monochromator (Horiba, iHR 550) equipped with a 300 lines per mm grating and a liquid nitrogen-cooled charge-coupled device camera.

Contact potential difference and surface photovoltage measurements were performed using a commercial KP020 Kelvin probe system from KP Technology under ambient conditions. For illumination, a 455 nm Thorlabs LED with the current adjusted to SPV signal saturation approximated at 5 mW cm^{-2}.

The electrical conductivity was evaluated using interdigitated Ti/Au (20 nm/80 nm) contacts produced via photolithography and e-beam evaporation. A Keithley 6517B was used to scan the potential and measure the current in dark conditions and under the illumination of an uncalibrated halogen lamp at full power settings.

Supporting Information

Supporting Information is available from the Wiley Online Library or from the author.

Acknowledgements

This project has received funding from the European Research Council (ERC) under the European Union's Horizon 2020 research and innovation programme (grant agreement no. 864234), from the Deutsche Forschungsgemeinschaft (DFG, German Research Foundation) under Germany´s Excellence Strategy – EXC 2089/1 – 390776260, and TUM.Solar in the context of the Bavarian Collaborative Research Project Solar Technologies Go Hybrid (SolTech). J.E. acknowledges funding by the Deutsche Forschungsgemeinschaft (DFG, German Research Foundation) – 428591260. J.E. and V.S. acknowledge support from the Bavarian Academy of Sciences and Humanities. S.S. acknowledges support from the Alexander von Humboldt Foundation.

Open access funding enabled and organized by Projekt DEAL.

Conflict of Interest

The authors declare no conflicts of interest.

Data Availability Statement

The data that support the findings of this study are available from the corresponding author upon request.

Keywords

charge carrier engineering, defect engineering, doping, optoelectronic properties, photoanodes, solar water splitting, tantalum nitride (Ta_3N_5)

Received: June 9, 2023
Revised: September 4, 2023
Published online:

[1] T. Takata, K. Domen, *Dalton Trans.* **2017**, *46*, 10529.
[2] D. H. K. Murthy, H. Matsuzaki, Z. Wang, Y. Suzuki, T. Hisatomi, K. Seki, Y. Inoue, K. Domen, A. Furube, *Chem. Sci.* **2019**, *10*, 5353.
[3] J. M. Morbec, G. Galli, *Phys. Rev. B* **2016**, *93*, 035201.
[4] J. Fu, F. Wang, Y. Xiao, Y. Yao, C. Feng, L.e Chang, C.-M. Jiang, V. F. Kunzelmann, Z. M. Wang, A. O. Govorov, I. D. Sharp, Y. Li, *ACS Catal.* **2020**, *10*, 10316.
[5] L. Cui, M. Wang, Y. X.u Wang, *J. Phys. Soc. Jpn.* **2014**, *83*, 114707.
[6] a) A. Dabirian, R. Van De Krol, *Appl. Phys. Lett.* **2013**, *102*, 33905; b) B. A. Pinaud, A. Vailionis, T. F. Jaramillo, *Chem. Mater.* **2014**, *26*, 1576.
[7] J. Eichhorn, S. P. Lechner, C.-M. Jiang, G. Folchi Heunecke, F. Munnik, I. D. Sharp, *J. Mater. Chem.* **2021**, *9*, 20653.
[8] S. Khan, M. J. M. Zapata, D. L. Baptista, R. V. Gonçalves, J. A. Fernandes, J. Dupont, M. J. L. Santos, S. R. Teixeira, *J. Phys. Chem. C* **2015**, *119*, 19906.
[9] Y. Xie, Y. Wang, Z. Chen, X. Xu, *ChemSusChem* **2016**, *9*, 1403.
[10] a) Y. Pihosh, T. Minegishi, V. Nandal, T. Higashi, M. Katayama, T. Yamada, Y. Sasaki, K. Seki, Y. Suzuki, M. Nakabayashi, M. Sugiyama, K. Domen, *Energy Environ. Sci.* **2020**, *13*, 1519; b) Y. Xiang, B. Zhang, J. Liu, S. Chen, T. Hisatomi, K. Domen, G. Ma, *Chem. Commun.* **2020**, *56*, 11843.
[11] T. Higashi, H. Nishiyama, V. Nandal, Y. Pihosh, Y. Kawase, R. Shoji, M. Nakabayashi, Y. Sasaki, N. Shibata, H. Matsuzaki, K. Seki, K. Takanabe, K. Domen, *Energy Environ. Sci.* **2022**, *15*, 4761.
[12] a) J. Fu, Z. Fan, M. Nakabayashi, H. Ju, N. Pastukhova, Y. Xiao, C. Feng, N. Shibata, K. Domen, Y. Li, *Nat. Commun.* **2022**, *13*, 729; b) M. Zhong, T. Hisatomi, Y. Sasaki, S. Suzuki, K. Teshima, M. Nakabayashi, N. Shibata, H. Nishiyama, M. Katayama, T. Yamada, K. Domen, *Angew. Chem.* **2017**, *129*, 4817.
[13] J. Xiao, S. Nishimae, J. J. M. Vequizo, M. Nakabayashi, T. Hisatomi, H. Li, L. Lin, N. Shibata, A. Yamakata, Y. Inoue, K. Domen, *Angew. Chem.* **2022**, *61*, e202116573.
[14] X. Zou, X. Han, C. Wang, Y. Zhao, C. Du, B. Shan, *Sustain. Energy Fuels* **2021**, *5*, 2877.
[15] Y. Wang, D. Zhu, X. Xu, *ACS Appl. Mater. Interfaces* **2016**, *8*, 35407.
[16] L. Pei, Z. Xu, Z. Shi, H. Zhu, S. Yan, Z. Zou, *J. Mater. Chem. A* **2017**, *5*, 20439.
[17] J. Xiao, J. J. M. Vequizo, T. Hisatomi, J. Rabeah, M. Nakabayashi, Z. Wang, Q.i Xiao, H. Li, Z. Pan, M. Krause, N. Yin, G. Smith, N. Shibata, A. Brückner, A. Yamakata, T. Takata, K. Domen, *J. Am. Chem. Soc.* **2021**, *143*, 10059.
[18] J. Feng, D. Cao, Z. Wang, W. Luo, J. Wang, Z. Li, Z. Zou, *Chem. Eur. J.* **2014**, *20*, 16384.
[19] Y. Xiao, Z. Fan, M. Nakabayashi, Q. Li, L. Zhou, Q. Wang, C. Li, N. Shibata, K. Domen, Y. Li, *Nat. Commun.* **2022**, *13*, 7769.

© 2023 The Authors. Advanced Functional Materials published by Wiley-VCH GmbH

16163028, 0, Downloaded from https://onlinelibrary.wiley.com/doi/10.1002/adfm.202306539 by University Modena, Wiley Online Library on [19/12/2023]. See the Terms and Conditions (https://onlinelibrary.wiley.com/terms-and-conditions) on Wiley Online Library for rules of use; OA articles are governed by the applicable Creative Commons License

[20] L. Pei, B. Lv, S. Wang, Z. Yu, S. Yan, R. Abe, Z. Zou, *ACS Appl. Energy Mater.* **2018**, *1*, 4150.
[21] Y. Kado, C.-Y. Lee, K. Lee, J. Müller, M. Moll, E. Spiecker, P. Schmuki, *Chem. Commun.* **2012**, *48*, 8685.
[22] S. S. K. Ma, T. Hisatomi, K. Maeda, Y. Moriya, K. Domen, *J. Am. Chem. Soc.* **2012**, *134*, 19993.
[23] S. H. Elder, F. J. Disalvo, L. Topor, A. Navrotsky, *Chem. Mater.* **1993**, *5*, 1545.
[24] G. Fan, X. Wang, H. Fu, J. Feng, Z. Li, Z. Zou, *Phys Rev* **2017**, *1*, 035403.
[25] Y. He, J. E. Thorne, C. H. Wu, P. Ma, C. Du, Q.i Dong, J. Guo, D. Wang, *Chem* **2016**, *1*, 640.
[26] a) F. Esaka, K. Furuya, H. Shimada, M. Imamura, N. Matsubayashi, H. Sato, A. Nishijima, A. Kawana, H. Ichimura, T. Kikuchi, *J. Vac. Sci. Technol., A* **1997**, *15*, 2521; b) C.-M. Jiang, L. I. Wagner, M. K. Horton, J. Eichhorn, T. Rieth, V. F. Kunzelmann, M. Kraut, Y. Li, K. A. Persson, I. D. Sharp, *Mater. Horiz.* **2021**, *8*, 1744.
[27] D. Cabaret, Y. Joly, H. Renevier, C. R. Natoli, *J Synchrotron Radiat* **1999**, *6*, 258.
[28] "XAFS spectrum of Titanium nitride", can be found under, https://doi.org/10.48505/nims.2452.
[29] a) A. Salamat, A. L. Hector, P. Kroll, P. F. Mcmillan, *Coord. Chem. Rev.* **2013**, *257*, 2063; b) V. S. Bhadram, H. Liu, E. Xu, T. Li, V. B. Prakapenka, R. Hrubiak, S. Lany, T. A. Strobel, *Phys. Rev. Mater.* **2018**, *2*, 011602.
[30] a) Z. Chen, T. F. Jaramillo, T. G. Deutsch, A. Kleiman-Shwarsctein, A. J. Forman, N. Gaillard, R. Garland, K. Takanabe, C. Heske, M. Sunkara, E. W. Mcfarland, K. Domen, E. L. Miller, J. A. Turner, H. N. Dinh, *J. Mater. Res.* **2010**, *25*, 3; b) J. A. Turner, *Chem. Ed.* **1983**, *60*, 327; c) D. K. Schroder, *Meas. Sci. Technol.* **2001**, *12*, R16.
[31] N. P. Barradas, C. Jeynes, R. P. Webb, *Appl. Phys. Lett.* **1997**, *71*, 291.
[32] A. Di Cicco, G. Aquilanti, M. Minicucci, E. Principi, N. Novello, A. Cognigni, L. Olivi, *J Phys Conf Ser* **2009**, *190*, 12043.
[33] E. A. Rozhkova, K. Ariga, *Molecules to Materials*, Springer, Midtown Manhattan, New York **2015**.

© 2023 The Authors. Advanced Functional Materials published by Wiley-VCH GmbH

16163028, 0, Downloaded from https://onlinelibrary.wiley.com/doi/10.1002/adfm.202306539 by University Modena, Wiley Online Library on [19/12/2023]. See the Terms and Conditions (https://onlinelibrary.wiley.com/terms-and-conditions) on Wiley Online Library for rules of use; OA articles are governed by the applicable Creative Commons License